



## OPEN Microstructural damage analysis during drilling in composite laminate with and without smart magneto-elastomer backup

Punit Patel<sup>1✉</sup>, Vijaykumar Chaudhary<sup>1</sup>, Dipal Patel<sup>1</sup>, Ramesh Upadhyay<sup>2</sup> & Sachin Patel<sup>3</sup>

CFRP is the most popular composite material due to its excellent mechanical properties. Most practical applications of CFRP in various industries require routine machining operations, such as drilling. Delamination of composites during drilling is a critical issue in high-end applications, caused by the thrust force generated throughout the drilling process. In this article, a magnetorheological elastomer (MRE)-based isolator is utilized during the drilling of CFRP to minimize the effects of thrust force. This study considers the impact of fiber orientation; thus, CFRP with unidirectional and bidirectional composites is employed for the drilling operation. An MRE-based isolator can equally reduce the thrust force in both uni-directional and bi-directional CFRP by the same percentage. An empirical model has been developed to explain the variation of thrust force concerning the last five layers of CFRP. The results demonstrate the influence of fiber orientation on magnetic-field induced thrust force. Nonetheless, a significant focus of this work is to elucidate the effect of thrust force reduction through microstructural evaluation of the drilled hole using a scanning electron microscope. Microstructural observations correlate with the analytical findings based on the empirical model. This study includes a layer-wise analysis of the effect of thrust force on drilled hole quality for both types of CFRP.

**Keywords** CFRP, Drilling, Magnetorheological elastomer, Microstructure analysis, Thrust force

### Abbreviations

$a$	Half of the delamination size along with fiber orientation
$a'$	Elastic coefficient
$dA$	Change in the area of delamination.
$B$	Magnetic flux density
$b$	Magnetic field-induced coefficient
$C$	Compliance factor
$h$	Thickness of uncut laminate
$H$	Total thickness of the laminate
$D$	Diameter of drill bit
$D_{ij}$	Bending stiffness matrix components
$P$	Total force
$PC$	Critical thrust force (CTF)
$P_E$	Elastic-field induced thrust force
$P_M$	Magnetic-field induced thrust force
$G_{1C}$	Energy release rate
$k$	Strain energy factor
$m$	Power exponent for magnetic field
$n$	Power exponent for stress
$t$	Thickness of the laminate
$t_B$	Bottom layer thickness

<sup>1</sup>Department of Mechanical Engineering, Faculty of Technology & Engineering (FTE), C. S. Patel Institute of Technology (CSPIT), Charotar University of Science and Technology, CHARUSAT Campus, Changa 388421, Gujarat, India. <sup>2</sup>Dr K C Patel Research & Development Centre, Charotar University of Science & Technology, CHARUSAT campus, Changa 388421, Gujarat, India. <sup>3</sup>P. D. Patel Institute of Applied Sciences, Charotar University of Science and Technology (CHARUSAT), Changa 388421, Gujarat, India. ✉email: punitpatel.me@charusat.ac.in

$dU$	Infinitesimal strain energy
$\tau$	Stress
$\xi$	Ellipticity ratio
$\alpha$	Contributing factor
$\vartheta$	Poisson's ratio
HSS	High-speed steel

Composite materials' outstanding mechanical strength compared to metal alloys have made them a superior candidate in various industries. Their significant impact is evident in the airframe, where nearly 50% of its weight is comprised of composite materials. Carbon fibre-reinforced plastic (CFRP) is the most used composite material due to its high load-bearing capacity and low weight-to-strength ratio compared to most metallic and non-metallic materials<sup>1,2</sup>. CFRP weighs only 40% as much as to aluminium<sup>3</sup>. CFRP laminate needs two types of machining processes, primary and secondary, to meet the functional requirements of aviation applications<sup>4,5</sup>. CFRP laminates are fabricated from raw material to the near net shape using various primary processes such as hand layup, autoclave molding, vacuum-assisted resin transfer molding, etc<sup>6</sup>. After that, various secondary processes are performed, like drilling, turning, and milling, to obtain the surface quality and close dimensional tolerance for the assembly of the complex parts<sup>7</sup>.

Drilling is considered the most suitable secondary machining process due to its advantages, with over 40% of machining time is allocated for drilling a medium-sized aircraft<sup>8</sup>. The need for structural joints mainly stresses drilling operations, which creates a serious threat of defects during the entry and exit of drill bits<sup>9</sup>. The defects at both entry and exit lower the bearing strength, thus requiring additional manufacturing processes to increase service life under fatigue loads<sup>10</sup>. In addition, due to the inhomogeneous and anisotropic characteristics of the material, drilling-induced damages lead to nearly 60% part rejection<sup>11</sup>. The number of defects primarily depends on the thrust force applied during the drilling process, as well as other factors such as drill geometry, materials, and feed rate<sup>12–19</sup>. Therefore, reducing the thrust force significantly reduces drilling-induced damage<sup>2,10,20</sup>.

Various researchers have made substantial efforts in tool optimisation and drilling conditions to suppress the thrust force<sup>21</sup>. Advanced drilling conditions include cryogenic cooling, pilot hole, passive spring-damper mechanism, and support plate mechanism<sup>2</sup>. In cryogenic cooling, various studies concluded that liquid nitrogen can increase the thrust force. Still, at the same time, surface roughness and hole quality are significantly improved compared to dry drilling conditions. Meanwhile, Mingzheng Liu et al. concluded that cryogenic cooling with minimal lubrication can significantly reduce the thrust force and drilling temperature<sup>22</sup>. However, this method relies on cryogenic cooling equipment such as low-temperature refrigerators or portable air-cooled guns.

Recently Wang et al. proposed three different arrangements of pilot holes for high-speed drilling of thin CFRP<sup>23</sup>. It was noticed that the thrust force can be reduced up to 55% when a 1 mm pilot hole is drilled. Despite this advantage, the pilot hole approach faces challenges with alignment issues and the time required to prepare the drilling specimen. The support plate mechanism<sup>24</sup> is a practical and widely used technique to enhance hole quality in CFRP. Many researchers have worked on various backup support mechanisms, including active backup, passive backup, stack backup and fabricated backup<sup>25</sup>, over the past few years. Dogrusadik et al. performed micro-drilling experiments using phenolic and wooden plates as stacks<sup>26</sup>. It is observed that the wooden plate reduced the thrust force because of the softness of the stack. Shyha et al. prepared a CFRP laminate with a glass scrim and nylon peel ply on the front and back surfaces<sup>27</sup>. It observed a similar pattern in thrust force behaviour, but superior hole quality was observed due to the nylon-fabricated backup. The passive backup's thrust force is significantly increased compared to the conventional experiment. Meanwhile, the surface of the drill quality is severely damaged due to the sudden impact of the thrust force on the microstructure of a laminate. In a recent study, Wang et al. proposed a passive backup support using the mechanical spring-damper mechanism to reduce thrust force during drilling in CFRP laminate<sup>28</sup>. The drilling experiments were performed on a 16-layered CFRP laminate using a 5 mm solid carbide twist drill with and without mechanical spring-damper support. Under spring-damper support, resulting in a 25% reduction in thrust force.

For the active backup support, John et al. introduced active spring restoring backup force using solid springs during drilling in CFRP laminate under variable feed rate (100–300 mm/min) and cutting speed (2000–4000 rpm)<sup>29</sup>. The experiment results revealed that active backup support increases the magnitude of thrust force due to the reaction force from the solid spring material. On the contrary, the exit layer deformation rate is considerably reduced irrespective of the advancement in the thrust force. Tsao et al.<sup>30</sup> performed experiments to study the effect of active backup on CFRP laminates using a tubular solenoid electromagnet. The observation suggests that the thrust force with active backup is significantly elevated compared to those without backup conditions, and the exit layer deformation rate is reduced by up to 80% using active backup support. Later, Hochang et al.<sup>31</sup> proposed inexpensive magnetic colloid material as an active backup support in the tube underneath the drilling specimen. The experimental results revealed that thrust force increased; however, drilling-induced damage was reduced marginally in the last couple of layers of the CFRP laminate.

Various researchers have designed and developed MRE-based isolators to absorb vibration<sup>32,33</sup>. A few have developed active or semi-active squeeze, compression, and mixed-mode MRE-based isolators for multiple applications<sup>34,35</sup>. Recently Wang et al.<sup>36</sup> developed MRE-based isolator for absorbing thrust forces in airborne applications and validated its performance through mathematical modelling. MRE-based isolators work as vibration isolators and absorb the thrust force. Most of the research primarily focused on structural vibration isolation. However, the application in reducing the thrust force and delamination in drilling applications is not being studied. Thus, the present investigation will be an added advantage of MRE-based devices in drilling applications.

Recently, our group has proposed a unique solution for reducing drilling-induced damage at both the entry and exit levels, using smart magnetorheological elastomer (MRE) as an active backup in one-directional CFRP

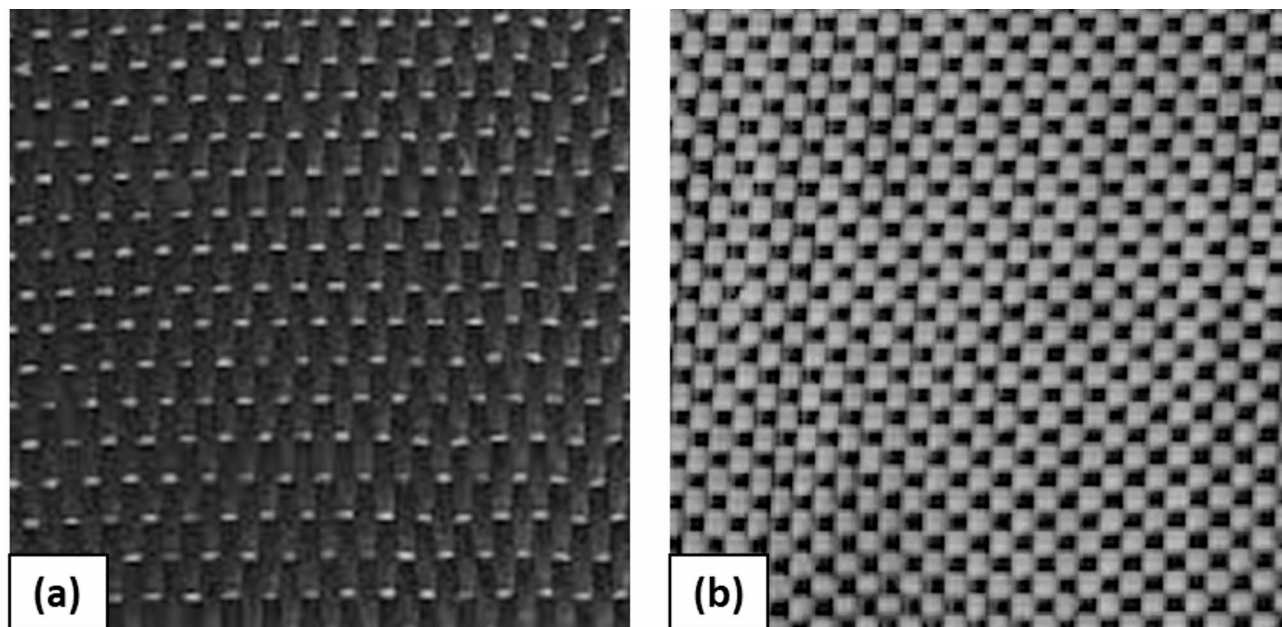


**Fig. 1.** Types of carbon fibre laminate used in the present study: (a) Unidirectional carbon fibre (CTC1-FUD160), (b) Bidirectional carbon fibre (CTC1-FBD400).

Parameters	CTC1-FUD160	CTC1-FBD400
Thickness of fibre (mm)	$0.16 \pm 0.03$	$0.42 \pm 0.03$
Tensile strength (MPa)	3.53	4.9
Tensile modulus (GPa)	230	240
Wave style	Unidirectional	Bidirectional
Density (g/cc)	1.8	1.8

**Table 1.** Basic Raw materials properties used to prepare CFRP.

composite<sup>37</sup>. In the study, it was observed that introducing MRE as an active backup reduces the thrust force and drilling damage. The reduction in thrust force is 30%, while damages at the exit level (delamination) are 40%. The novelty of the present work lies in understanding the microstructural damage propagation within the composite layers under the MRE as an active backup. In particular, a focus is on the last few layers of the exit side, where maximum defects are expected due to increased thrust force. The microstructural damage propagation within the structure is reported using the scanning electron microscope (SEM) images. To better understand the influence of MRE on damage propagation, we have considered unidirectional and bidirectional composite materials for the analysis. The results show that using MRE as an active backup reduces the thrust force and delamination but hinders the damage propagation up to the last layer of composite materials.

## Materials and methods

### Fabrication of CFRP

In the present study, two identical CFRP composites were considered: unidirectional CFRP and bidirectional CFRP, as shown in Fig. 1. The raw materials used to prepare the composite and their parameters are listed in Table 1. Using the positive compaction method, the CFRP laminate was made using a 14-layer unidirectional carbon fibre (CTC1-FUD160) and composite-grade liquid epoxy resin (CT/E 556). The area density of unidirectional carbon fabric (CTC1-FUD160) is  $165 \pm 15$  g/m<sup>2</sup>. The unidirectional CFRP lamina contains carbon fibre in the wrap direction and EC9 non-alkali glass fibre yarn in the weft direction to provide the overall structural integrity. A detailed schematic diagram of the preparation method is shown in Fig. 2(a). For the positive compaction method, curing was carried out at 80°C temperature with 25 bar pressure for an hour and then rested at room temperature. The volume fraction was maintained at 0.59, and the unidirectional laminate (*t*) thickness was  $2.99 \pm 0.2$  mm.

On the other side, a bidirectional CFRP laminate was fabricated using a 12-layer bidirectional carbon fibre (CTC1-FBD400) and composite grade liquid epoxy resin (CT/E 556) using the vacuum-assisted resin transfer moulding (VARTM) method (Fig. 2(b)). The area density of bidirectional carbon fabric (CTC1-FBD400) is  $400 \pm 15$  g/m<sup>2</sup>. The bidirectional CFRP lamina contains carbon fibre in the warp and weft directions, resulting in higher structural strength than unidirectional CFRP. For the VARTM method, vacuum gauge pressure

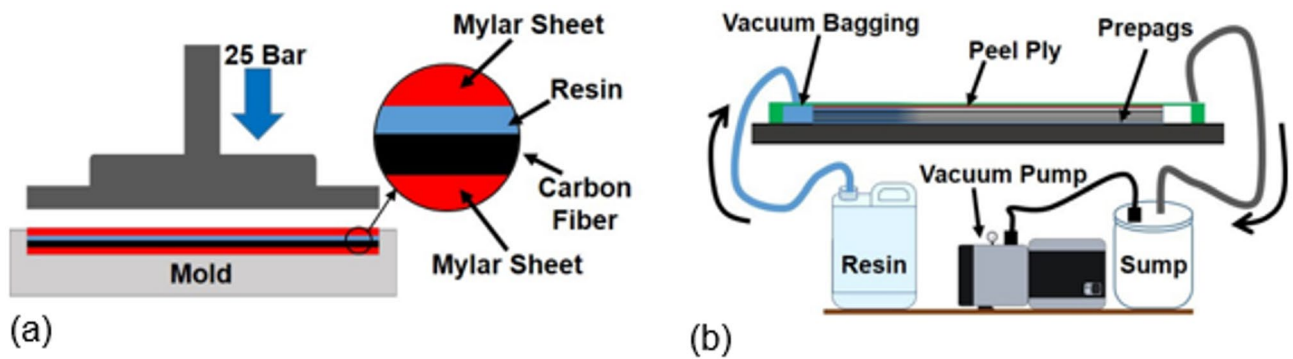


**Fig. 2.** (a) The Hand lay-up method with positive compaction technique and (b) vacuum-assisted resin transfer moulding method used for CFRP preparations.

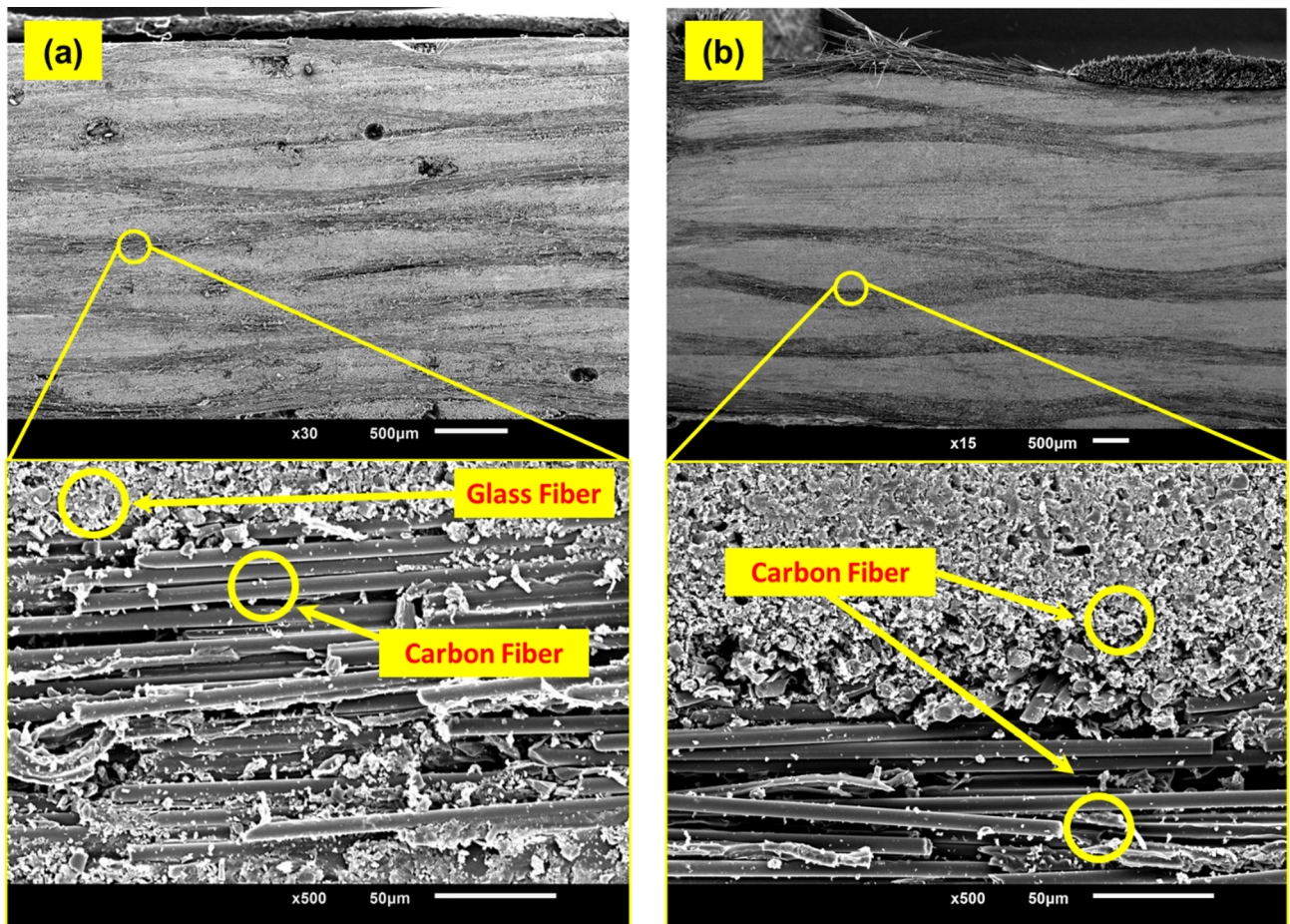


**Fig. 3.** SEM images of (a) Unidirectional CFRP and (2) Bidirectional CFRP. The bottom images are higher resolution views.

was maintained at  $-80$  kPa and followed by curing was done at room temperature. The volume fraction was maintained at 0.61, and the thickness of bidirectional laminate ( $t$ ) was  $5.00 \pm 0.1$  mm. Figure 3 presents an SEM image of a cut section of both laminates, which illustrates the microstructure of both unidirectional and bidirectional CFRP laminates. Then, the required specimens from both large CFRP laminates were cut to a size of 25 mm x 90 mm on CNC milling machining using a 6 mm HSS drill bit for further analysis.

#### Fabrication of isotropic MRE

Along with this, an isotropic magnetorheological elastomer (MRE) was fabricated using irregularly shaped electrolyte iron particles (EIP) (Industrial Metal Powders, Pune, India) and liquid silicon rubber (SR) RTV-1010

(Aditya Silicone, Delhi, India) (60/40%w/w). The fabrication process involved three main steps. First; the SR and EIP were mixed in a cylindrical plexiglass beaker in a proper proportion, and using a motorised mechanical stirrer at a constant speed of 250 rpm for 5 min under room temperature and then to accelerate the curing process, isocyanate compound catalyst was added in required proportion and then stir the mixture at a constant speed of 250 rpm for 5 min. Then, the mixture was degassed by placing the beaker in a vacuum chamber for 5 min. Finally, the mixture was poured into a 3D-printed plastic mould and left at room temperature without the application of a magnetic field for curing, as illustrated in Fig. 4. After the curing, a random MRE was cut from the mould using a coin master pipe cutter with a manganese blade to obtain the exact dimension of  $\phi$  25 mm. The dispersion of magnetic particles in the MREs was investigated using a scanning electron microscope (JEOL-JSM6010LA). Microstructure images are illustrated in the inset of Fig. 4. The white points indicate the presence of EIPs, while the black background shows the SR matrix. The particles are isotropically distributed in the matrix.

### Rheological properties of isotropic MRE

For active backup support, the storage modulus of an innovative material is crucial, as it is directly related to the energy absorption rate. Various rheological properties were studied for the developed isotropic MRE using a rheometer. Figure 5(a) shows the rotational rheometer, Physica MCR 301 (Anton Paar, Graz, Austria), used to measure MRE's visco-elastic properties. A magneto-cell (Physica MRD 180/1T) was attached to the rheometer for magnetorheological measurements. The coil current varied from 0 A to 4 A, and the corresponding magnetic field intensity was recorded. The variation is linear in this range; magnetic field intensity varying from 0.016 mT to 640 mT. All the data were recorded at 300 K. The sample thickness was  $1.02 \pm 0.02$  mm. A parallel plate geometry (PP20) with a diameter of 20 mm and a gap of 1 mm was used. The magnetic field was applied normally to the sample.

Figure 5(b) shows the variation of storage and loss modulus with strain at different magnetic field intensities. The magneto-field-induced changes in storage modulus are visible in Fig. 5(b). The graph shows that in the presence of an electromagnetic field, the iron particles are aligned in the direction of the field, ultimately improving storage modulus. A higher storage modulus means a higher capacity to absorb thrust force. Similarly, the loss factor indicates the viscous dissipation of the material. An increase in the loss modulus with the field suggests that the viscous energy has increased. This increase may be due to the higher friction between the particles because of the shape. However, the loss factor remains constant till the linear viscoelastic region (1% strain) is reached; thereafter, the loss factor increases.

### Drilling experiment setup and drilling conditions

Drilling experiments were performed on a high-precision computer numerical control (CNC) operated drilling machine (JYOTI, PX10). Earlier research<sup>38</sup> considered a three-level L27 orthogonal array with three process parameters: point angle, feed, and cutting speed for drilling operations on CFRP laminate to optimise the drilling conditions. The influence of the various process parameters on thrust force was studied using statistical analysis and rigorous experimental methods. The optimised process parameters were 90° point angle, 0.07 mm/rev feed rate and 7500 rpm cutting speed. These optimised parameters were used in the present study. All tests were conducted under dry conditions at a fixed spindle speed of 7500 rpm and feed rate of 0.07 mm/revolution, using a 4.0 mm diameter standard HSS drill tool under atmospheric temperature and pressure. Meanwhile, the rheological properties of MRE can be tuned using a direct current (DC) supply, which is achieved using a

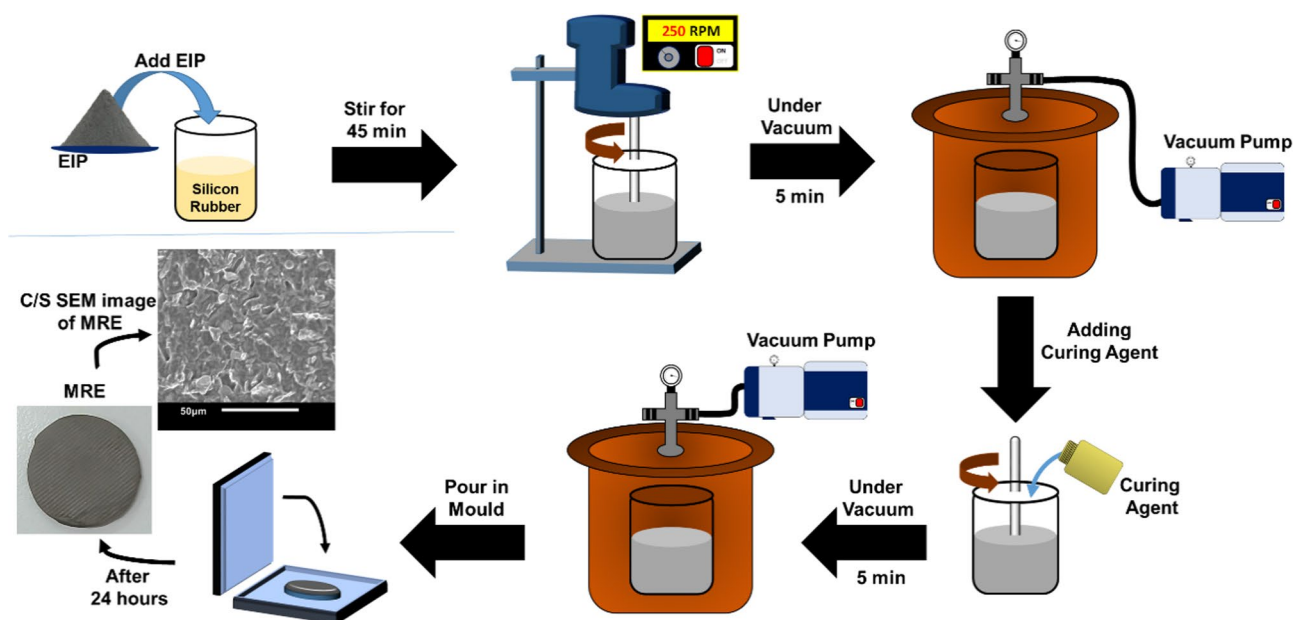
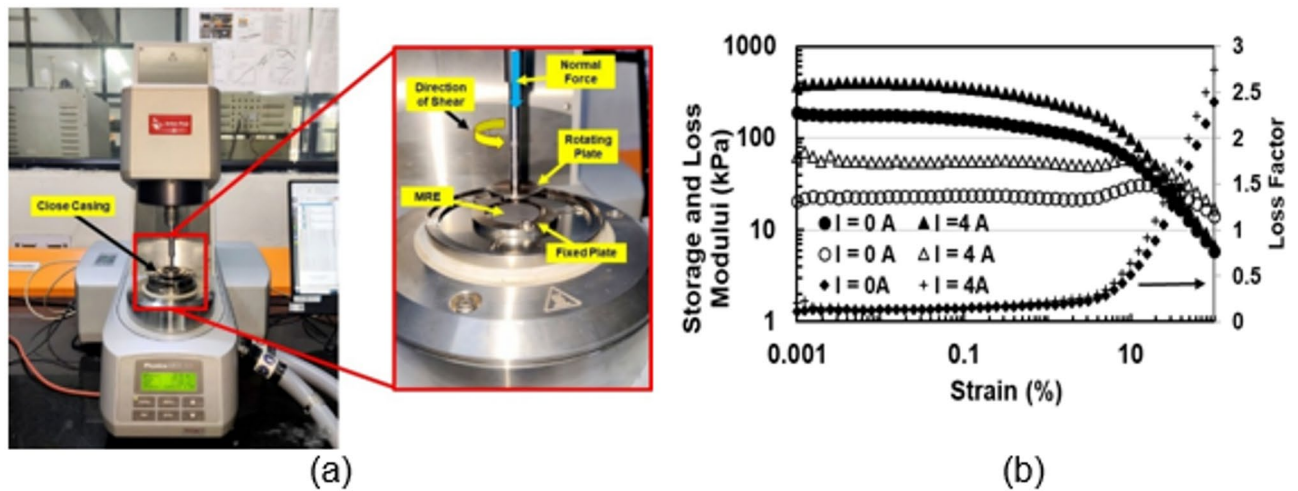
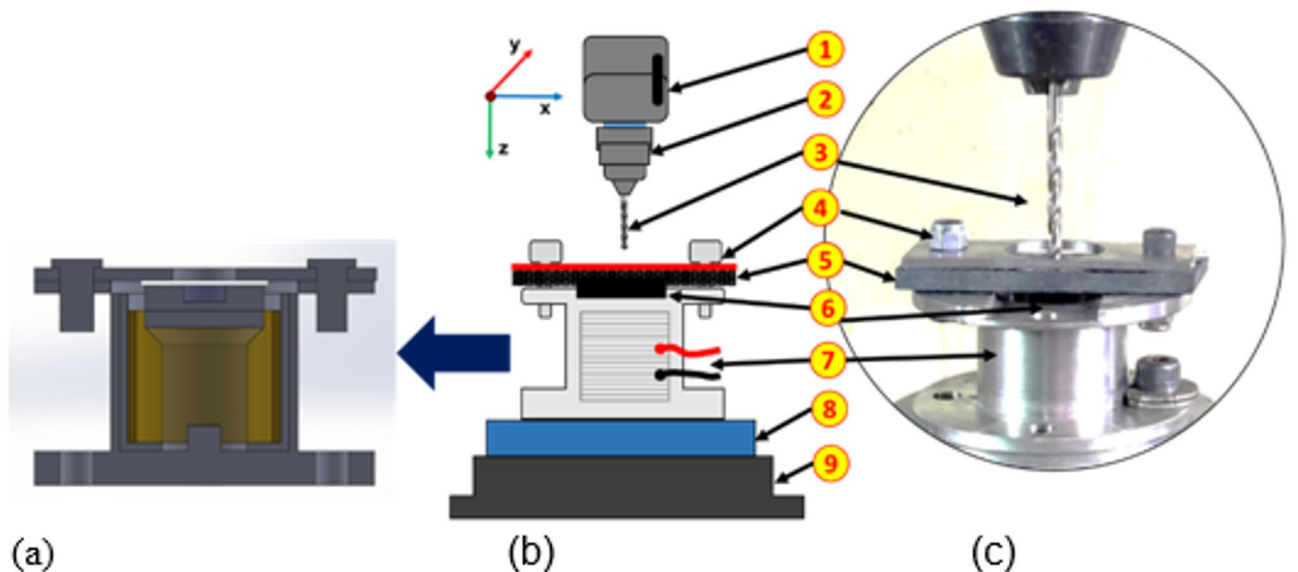


Fig. 4. Procedural layout of the fabrication of an isotropic MRE.



**Fig. 5.** (a) Anton-Paar Rheometer and zoom part of the sample stage used in the present research. (b) Variations of storage modulus (●,▲), loss modulus (○, △) and loss factor (◆, +) versus strain at two different current values recorded at 300 K. Loss factor is the right side vertical axis.



**Fig. 6.** (a) The cross-section view of the designed MRE mount, (b) Schematic view of experimental setup with details. (1) Chuck, (2) Spindle, (3) Drill bit, (4) Locating plate, (5) CFRP specimen (6), Isotropic MRE (7), Specially designed fixture (8), 4-component dynamometer (9), Mounting bed, and (c) actual set up image.

regulated DC power supply (Range: 0–32 V and 0–5 A). The thrust force was measured using a Kistler-9272 4-component piezoelectric dynamometer, and the NI9221 analogue input module used to convert dynamometer signals into digital form. The real-time thrust force was measured at every 0.05-second interval, and the variation in the values was plotted as a waveform. The experimental setup is illustrated in Fig. 6. Figure 6(b) illustrating the schematic diagram of an experimental setup.

A specially designed fixture<sup>37</sup> is shown in cross-section in Fig. 6(a), and the actual image is shown in Fig. 6(c). It was firmly mounted on a dynamometer to transmit the load to the piezoelectric transducer, which was then used for real-time measurement. The fixture contained a magnetic coil made of insulated 26 SWG wire, used to tune the rheological properties of MRE. Once the workpiece is mounted on top of the fixture, the DC supply is regulated as per the test condition, and the electrical supply is turned off when drilling is completed. During drilling operations, tuned MRE provides active backup. All drilling experiments were performed under three different test conditions, as described in Table 2.

Each experiment was repeated three times under the same conditions to verify the reproducibility, and the average value was used for analysis. The thrust force curves are smoothed using the Savitzky-Golay filter approach to reduce noise in the signal. Figure 7 presents a typical thrust force curve recorded three times and the

Exp. No.	Process Parameters			
	Point Angle (Degree)	Feed rate (mm/rev)	Cutting Speed (rpm)	Special Condition
1	90	0.07	7500	Default setup
2	90	0.07	7500	MRE (B = 0 T)
3	90	0.07	7500	MRE (B = 0.48 T)

**Table 2.** Process parameters for machining conditions.

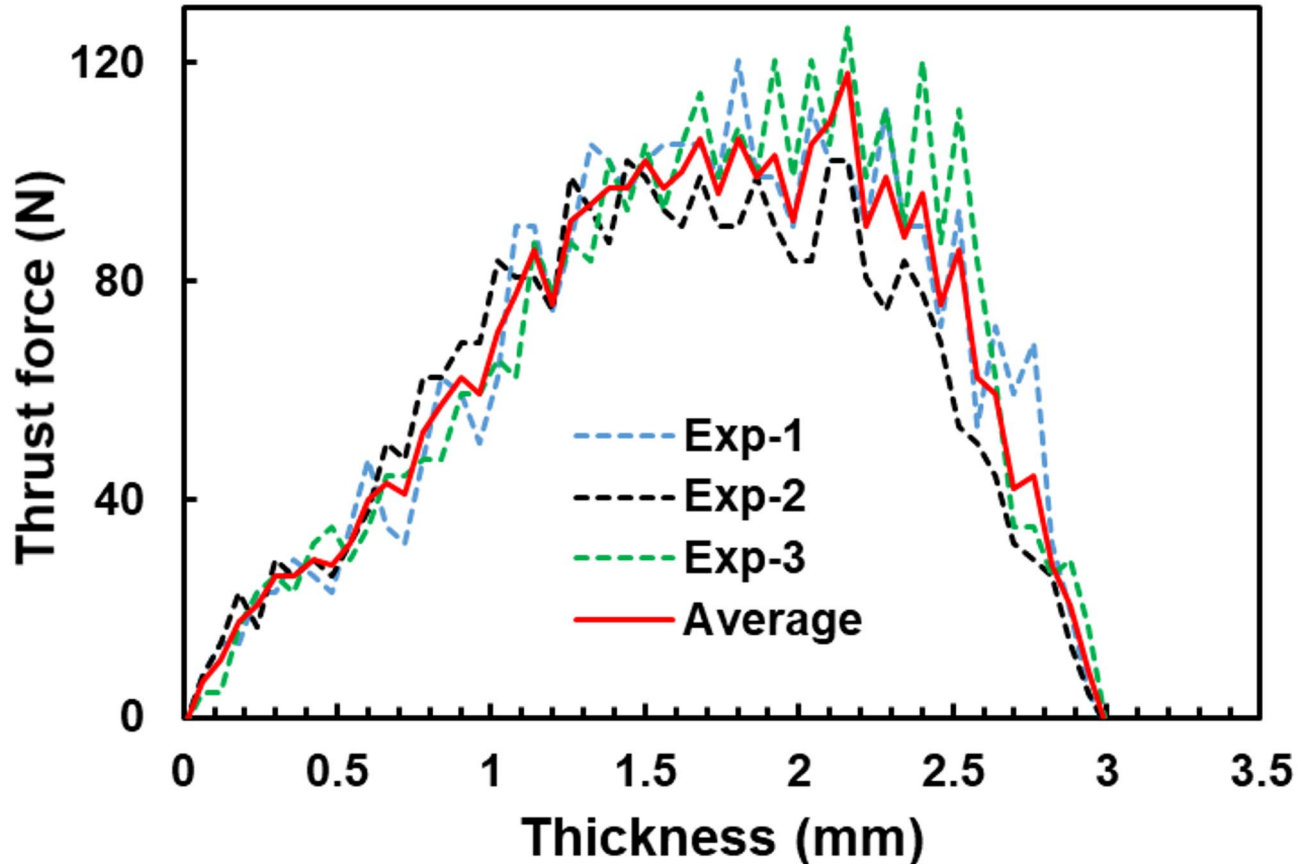


**Fig. 7.** Typical thrust force versus thickness curve for CFRP with MRE active back-up to confirm the reproducibility.

average curve. The figure clearly indicates a high level of result reproducibility. The same procedure was adopted for all the measurements reported here at every condition listed in Table 2.

### Mechanism to understand the thrust force reduction by active MRE backup

#### Basic model for thrust force reduction

Thrust force is generated due to the drilling tool's axial action and the downward spiral movement, which induces material delamination<sup>2,10,39</sup>. The thrust force acting through the drill bit can be predicted numerically using three theories: linear elastic fracture mechanics (LEFM)<sup>40,41</sup> classical plate theory (CPT)<sup>42</sup> and engineering mechanics of composite materials<sup>43,44</sup>. Each theory influences the total downward force. A theoretical analysis for critical thrust force proposed by Ho-chang<sup>45</sup> written as Eq. (1).

$$P_C = \pi \sqrt{\frac{8G_{1C} E h^3}{3(1-\nu^2)}} = \pi \sqrt{32G_{1C} M} \quad (1)$$

Here,  $P_C$  represents CTE,  $G_{1C}$  represents strain energy release rate,  $E$  and  $\nu$  represent Young modulus and Poisson's ratio of the materials, respectively.  $M$  is the flexural rigidity of the reinforced composite material, and  $h$  is the thickness of uncut laminae beneath the tool. During delamination propagation, the drill movement of

distance ( $dx$ ) is associated with the work done by the thrust force ( $P_c$ ) on the workpiece, which deflects the plate and propagates the inter-laminar crack. The energy balance gives,

$$P_C dX = G_{1C} dA + dU \quad (2)$$

In this context,  $dA$  is the change in crack propagation area, and  $dU$  is the infinitesimal strain energy of the defined limit. Recently, Patel et al.<sup>46</sup>, proposed a mathematical model to predict thrust force in a unidirectional CFRP composite. According to this model, total load exerted ( $P_C$ ) is the sum of the point load ( $F_1$ ) exerted by the drill tip and the chisel load ( $F_2$ ). The thrust force can be calculated numerically for an elliptic shape delamination. Meanwhile, the uniformly distributed load acts through chisel edges during drilling. According to this model, the effect of the extensional stiffness matrix and coupling stiffness matrix components is zero for unidirectional composite specimens due to the laminate's symmetry, and thus the effect of the fibre cutting angle (FCA) is neglected. However, the bending stiffness matrix (a  $3 \times 3$  matrix defines the numerical value of the stiffness components), two elements,  $D_{16}$  and  $D_{26}$ , are generally zero as all laminates are placed at 0 degrees. Using this model, the expression for strain energy can be found by solving the above equation with a limit of integration:

$$U = \frac{P_C a^2 \xi}{9\pi [D_{11} + \frac{2\xi^2}{3} (D_{12} + 2D_{66}) + D_{22}\xi^4]} \quad (3)$$

$$U = F_1^2 k a^2 + F_2^2 k a^2 = [\alpha^2 + (1 - \alpha)^2] \frac{F^2 a^2 \xi}{9\pi D^*} \quad (4)$$

$$P_C = F_1 + F_2 = \alpha F + (1 - \alpha) F \quad (5)$$

Similarly, by integrating the displacement term  $dx$ ,

$$X = F_1^2 C_3 a^2 + F_2^2 \frac{C_3}{3} a^2 = [3\alpha^2 + (1 - \alpha)^2] \frac{F^2 a^2 \xi}{18\pi D^*} \quad (6)$$

Finally, substituting Eqs. (5) and (6) into Eq. (2) gives an expression as follows:

$$P_C = \frac{3\pi}{\xi} \sqrt{\frac{2G_{1C} (D_{11} + \frac{2}{3} (D_{12} + 2D_{66}) \xi^2 + D_{22}\xi^4)}{2\alpha - 1}} \quad (7)$$

The simpler version of this equation is;

$$P_C = \frac{3\pi}{\xi} \sqrt{\frac{2G_{1C} D^*}{2\alpha - 1}} \quad (8)$$

Where,  $D^* = D_{11} + \frac{2}{3} (D_{12} + 2D_{66}) \xi^2 + D_{22}\xi^4$

Numerical calculations were performed for the default set-up (i.e., without MRE backup) by substituting the parameter values.

#### Model incorporating active MRE backup

Figure 8 shows the schematic diagram used to explain the mechanism of active backup. The active backup provided at the bottom of the plate helps absorb the thrust force, which varies with the magnetic field. It is known that in a zero magnetic field, the MRE behaves as an elastic material. Therefore, the damping property of the elastomer will play a role in absorbing the thrust force. The elastic property of MRE was studied using a rheometer, and the stress value at different strains was measured.

The stress saturates at a strain above 1%, and the value thus obtained was 1876 N. In Eq. (1), the elastic constant varies as a power of  $\frac{1}{2}$ . Considering the similar variation, one more term is added in Eq. (8) to account for the effective elastic contribution ( $P_E$ ), and the total thrust force ( $P$ ) is expressed as;

$$P = P_C + P_E = P_C + a' \tau^n \quad (9)$$

Here,  $a'$  and  $n$  are variables. However, as mentioned earlier, the power  $n$  is taken as  $\frac{1}{2}$ . Using Eq. (9), the value of  $a'$  for the thrust force with MRE backup was obtained.

Under the influence of a magnetic field, MRE exhibits magnetic field-induced changes in its elastic stress. It has been reported that the variation of stress with a magnetic field is nonlinear and generally obeys a power law with a power of  $3/2$ <sup>47</sup>. The influence of magnetic-field-induced stress suppresses the thrust force, thus reducing the crack propagation till the last layer. Hence, Eq. (9) is extended by incorporating magnetic-field induced thrust force ( $P_M$ ) and rewritten as,

$$P(B) = P_C + P_E + P_M = P_C + a' \tau^n + bB^m \quad (10)$$

The power  $m$  is considered to be  $3/2$ .

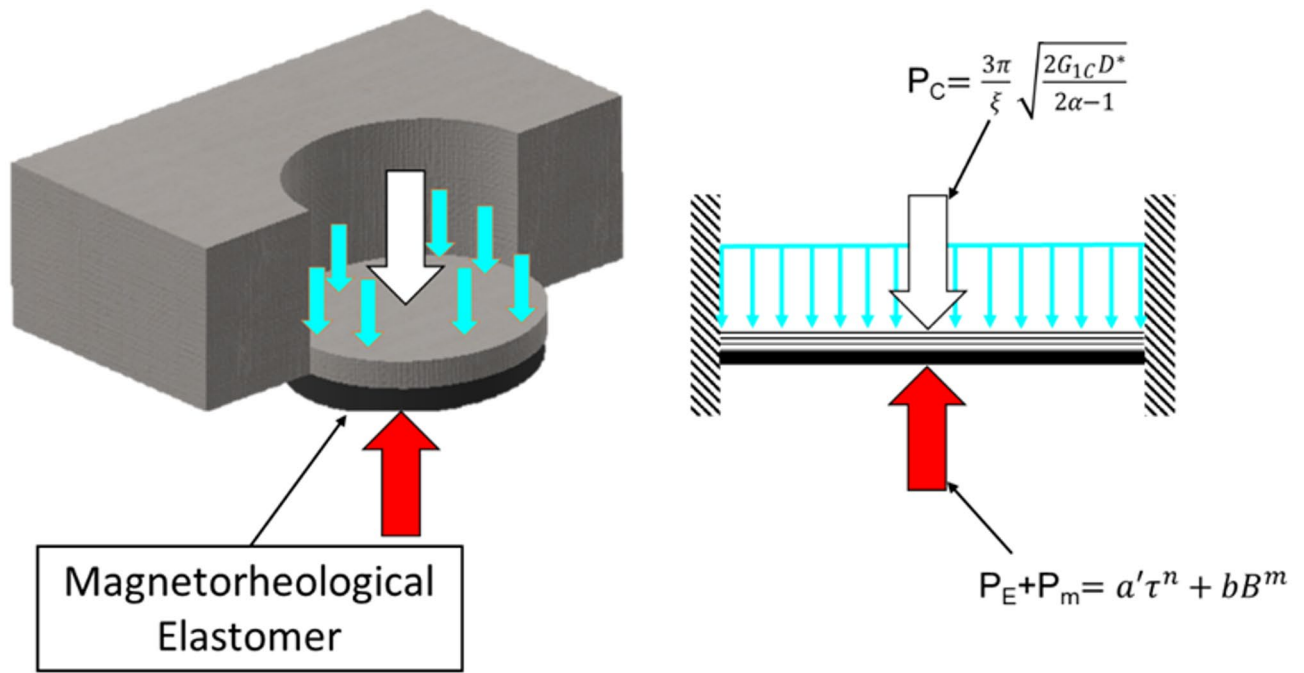


Fig. 8. A schematic diagram is used to explain the basic mechanism and model.

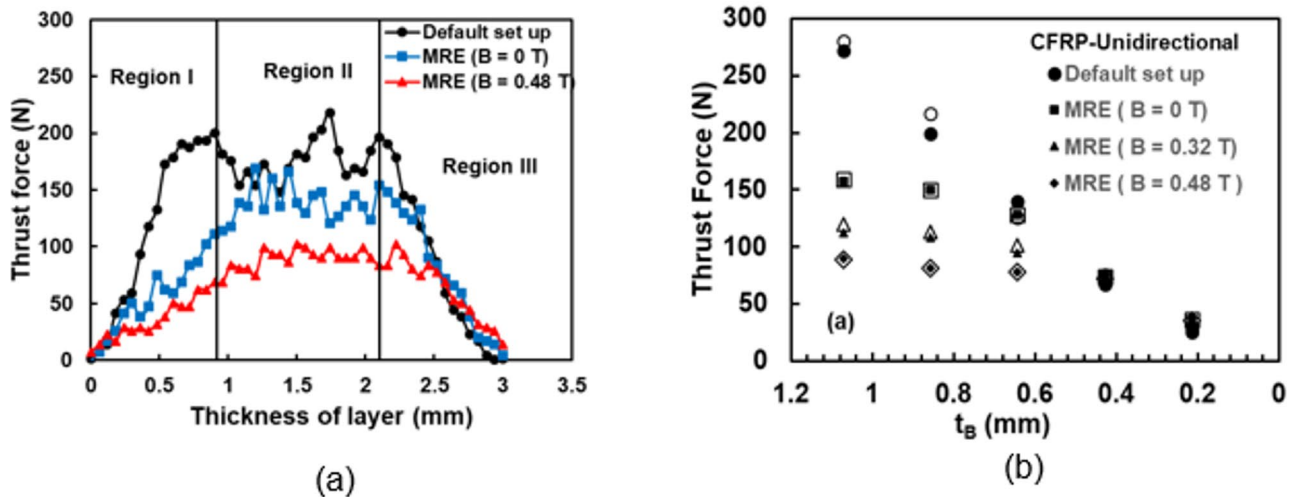


Fig. 9. (a) Variation of thrust force with thickness of layer and (b) variation of thrust force values derived from bottom layer thickness,  $t_B$ , (i.e. region III) for default and MRE at different fields. The filled symbols are experimental, and the open symbols are calculated values using the Eq. (10).

## Results and discussion

### Thrust force variation for unidirectional composite

The thrust force variation for unidirectional CFRP was studied both with and without active back-up force. Figure 9(a) shows the behaviour of thrust force and the thickness of the laminate (in the drilling direction) during the drilling operation for a unidirectional laminate. Three regions were defined: Region 1, which indicates the portion of the drilling operation where the drill tool enters the workpiece. In this region, for all conditions, the rate of increment of thrust force is nearly linear for the initial drilling operation, irrespective of the slope value. After that, in Region 2, the internal layers' penetration of the drilling tool, the thrust force varies in a particular range. Lastly, in Region 3, the thrust force decreases when the drill reaches the last lamina.

Figure 9(a) shows that the thrust force value fluctuates between 150 N and 215 N for the default setup and is reduced to 80 N to 100 N for MRE with 3 A drilling conditions. The thrust force values were obtained from Fig. 9(a) for the default set-up and MRE at different magnetic fields for the last five layers (region III). The variation of thrust force with bottom layer thickness and magnetic fields is shown in Fig. 9(b). Maximum thrust

force values were reduced by 22.5% from 218.11 N under the influence of MRE without a magnetic field in unidirectional CFRP (Fig. 9(a)). This reveals that MRE behaves like an elastic material and can absorb the thrust force during this condition. Meanwhile, increasing magnetic field intensity (0.48 T) for the same composite material reduced the maximum thrust force value by 30% from 169.27 N to 118.59 N. The reduction in thrust force is because of the tunable damping characteristic of an innovative material. Compared to the default condition, the maximum thrust force is reduced by 45% using smart magneto-elastomer backup at a 0.48 T magnetic field.

Equation (10) was used to simulate the values for the default set-up to explain the variation of thrust force with laminate thickness. The open symbol (○) in Fig. 9(b) represents the simulated values. The simulated results agree well with experimental values. To obtain the fit parameters for the field-induced changes in thrust force, initially, with MRE active back-up, at  $B = 0$  T, was calculated using Eq. (10), to obtain the coefficient  $a'$ . The open symbol (□) in Fig. 9(b) fits the Eq. (10). Once the values of the first two terms were obtained, the field-induced changes in the thrust force were calculated using Eq. (10) for different magnetic field values. The obtained values are shown in Fig. 9(b) as open symbols. The agreement between the experimental and calculated values supports the concept of magnetic-field-induced reduction of thrust force when MRE is used as active back-up.

The observed reduction in thrust force is also reflected in the delamination factor. To measure the delamination factor and to quantify the delamination damage due to thrust force, a 3D microscopy is used due to its simplicity. Digital images of the drilled holes were captured using a 3D microscope (Mitutoyo, QS-L2010ZB), and these images were then converted into binary format using ImageJ (version 1.53), open-licensed software (available at <https://imagej.net/ij/>)<sup>46</sup>. The two-dimensional push-out delamination factor is calculated using MATLAB code. Figure 10 shows a comparative study for push-out delamination for unidirectional CFRP laminate for all machining conditions (inset: original images for push-out delamination). Some uncut fibres visible in the digital images are associated with peel-up delamination. It is clear from Fig. 10 that the delamination factor is reduced with active MRE backup at 0 T and 0.48 T magnetic fields compared to the default setup.

### Thrust force variation for bidirectional composite

It is observed that bidirectional laminate needs more thrust force to drill than unidirectional laminates (Fig. 11(a)) because fibres are oriented multi-directionally, which can resist the load coming from various directions<sup>48</sup>. However, thrust force variation follows a similar pattern to that of unidirectional CFRP, under the same drilling conditions, irrespective of the force value. A similar pattern is also observed in Fig. 11(a), where the thrust force, for the default setup, varies between 180 N and 300 N, and at 0.48 T, it varies between 75 N and 160 N. In the case of bidirectional, the slope of Region 1 changes with MRE and in-field (with current), and it differs in rate of change compared to unidirectional MRE. However, the percentage change in thrust force with MRE remains nearly identical, indicating that the backup force is the same in both cases.

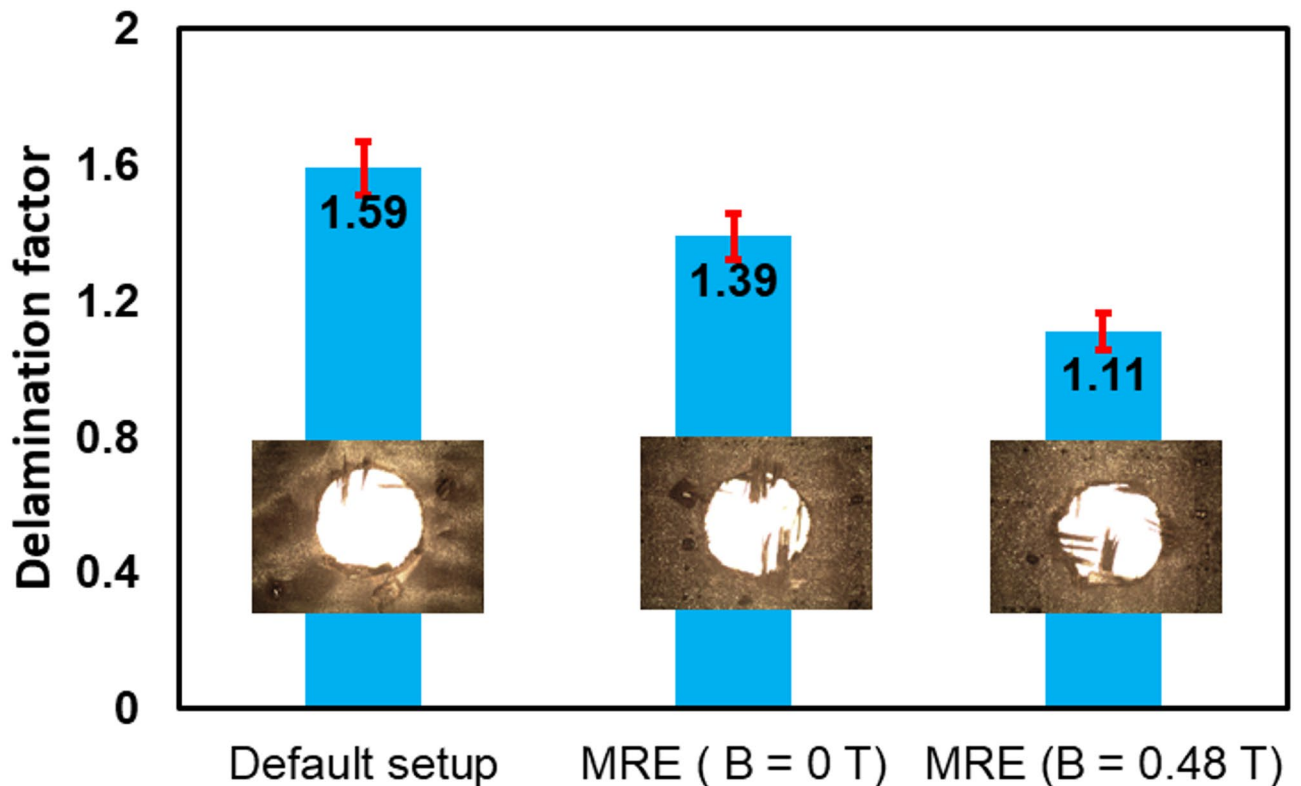


**Fig. 10.** The variation of the delamination factor with different experimental conditions. The inset in each bar shows the optical image of the delamination.

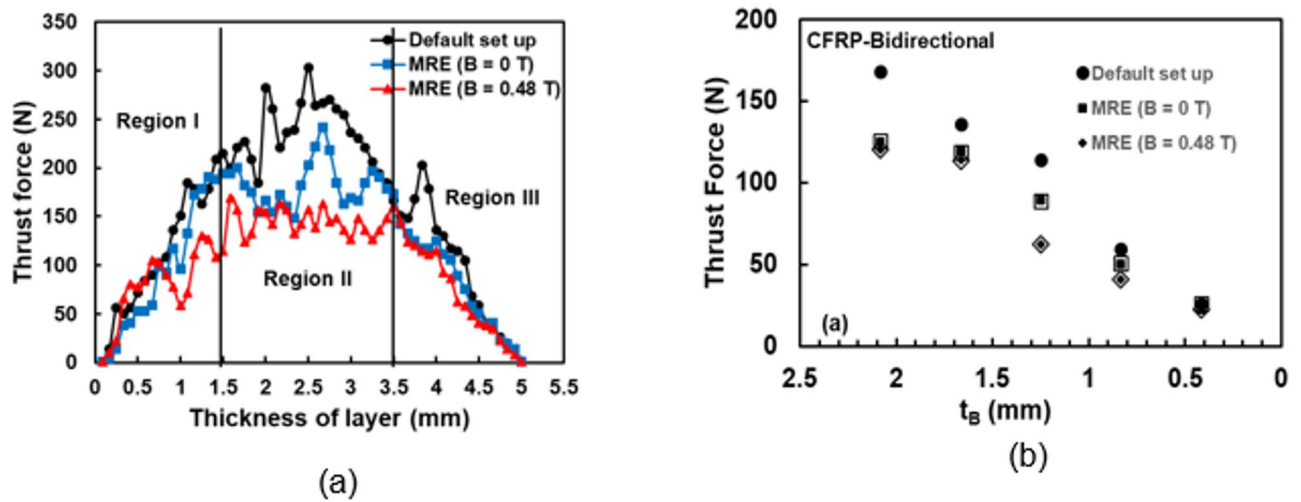


**Fig. 11.** Variation of thrust force with thickness of layer in bidirectional CFRP (a) and (b) variation of thrust force values derived from bottom layer thickness,  $t_b$ , (i.e. region III) for default and MRE at different fields. The filled symbols are experimental, and the open symbols are calculated values using the Eq. (10).

Similarly, Fig. 11(b) compares the maximum thrust force for bidirectional CFRP under various test conditions. For bidirectional CFRP laminate, maximum thrust force values were reduced by 20% when MRE was used. Compared to the previous scenario, 2.5% less thrust force was observed, possibly because of the higher cross-linking of carbon fibre in the bidirectional laminate. At 0.48 T magnetic field, the maximum thrust force value was reduced by 28% compared to the zero magnetic field value. The reduction in thrust force also advocates the tunable damping characteristic of a smart magneto-elastomer. Overall, 43% of the thrust force is absorbed by MRE under a magnetic field. It shows that the smart magneto-elastomer backup eliminates vibration and gradually absorbs the energy of the thrust force.

The experimental values of thrust force variation with magnetic field at each bottom layer thickness were compared to Eq. (10) and are shown in Fig. 11(b) as open symbols. The relation holds even for bidirectional CFRP with MRE as active backup.

#### Fit parameters variations between Uni and bi-directional CFRP

The percentage change in thrust force under MRE as an active backup for Uni and bi-directional CFRP remains nearly the same, as evident from Figs. 10 and 11. However, the variations in magnetically induced force parameters are different in both CFRPs. The figure compares the uni- and bi-directional CFRP fit parameter variation with bottom layer thickness. It is to be noted that both the CFRP have different thicknesses, but the experimental conditions are the same.

It is apparent from Fig. 12 that the fit parameter  $a'$  varies with bottom layer thickness, which is primarily a contribution of the elastic force on the CFRP with MRE as an active backup force. In calculating the second term in Eq. (10), the stress value was taken as 1.8 kN (which was kept the same for Uni and bi-directional CFRP) and the exponent as  $n = 0.5$ . However, the parameter  $a'$  was varied to get best fit. In both cases, the  $a'$  decreases as the drill approaches the last bottom layer. The CFRPs differs in the thickness of each layer because of the number of layers. The bidirectional CFRP has a higher Young's modulus than the unidirectional, as a result, the elastic component of MRE influence will be different, and the same is exhibited in the value of  $a'$  (Fig. 12).

In contrast, the variation of the  $b$  parameter (magnetic field-induced thrust force coefficient) behaves differently (Fig. 12- Inset). The field-induced values exhibit a maxima behaviour in bidirectional while in unidirectional it shows saturating and falling rapidly when the last laminate layers are approached. The magnitude of the  $b$  value is nearly half. Figure 13 compares the magnetic-field induced variation coefficient with the bottom layer thickness. It seems that almost half the thickness, the fit parameter value is maximum and decreases rapidly thereafter. At present, it isn't easy to understand the nature. However, it can be argued that because the other operational conditions are the same (like thickness of MRE, field values), the field-induced effect may be subject to layer thickness. It may not influence region II (refer to Figs. 9 and 11). A detailed study is needed for better understanding. In conclusion, the active MRE backup reduces the thrust force even if CFRP is unidirectional or bidirectional by a similar percentage. To better understand this behaviour, microscopic analysis was performed on both CFRP. The following section describes the microstructure analysis of the MRE.

#### Microstructure damage analysis of MREs during drilling

Scanning electron microscope (SEM) experiments were performed on the unidirectional and bidirectional CFRP laminate samples to understand the micro-level drilled quality and region-wise damage of the drilled hole. A cross-section of the drilled hole samples was examined using SEM for the experiments.

Figure 14 compares the SEM images of unidirectional CFRP under default set-up (WO) and MRE with 0.0 T along with binary images of peel-up and push-out delamination. The yellow marking and percentage

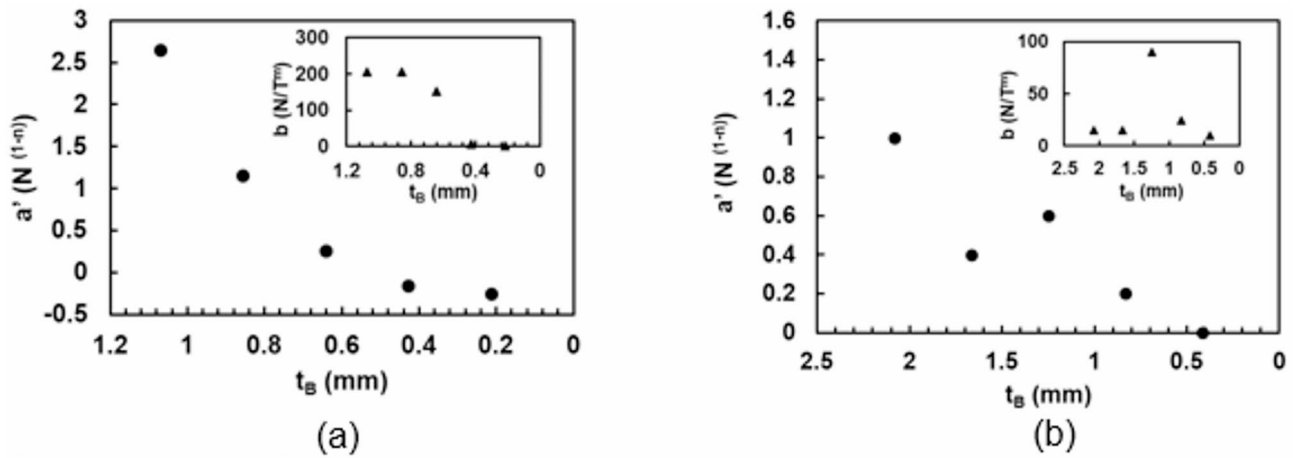


Fig. 12. Variation of obtained fit parameters with bottom thickness layer (a) for uni-directional and (b) bidirectional CFRP using Eq. (10) respectively.

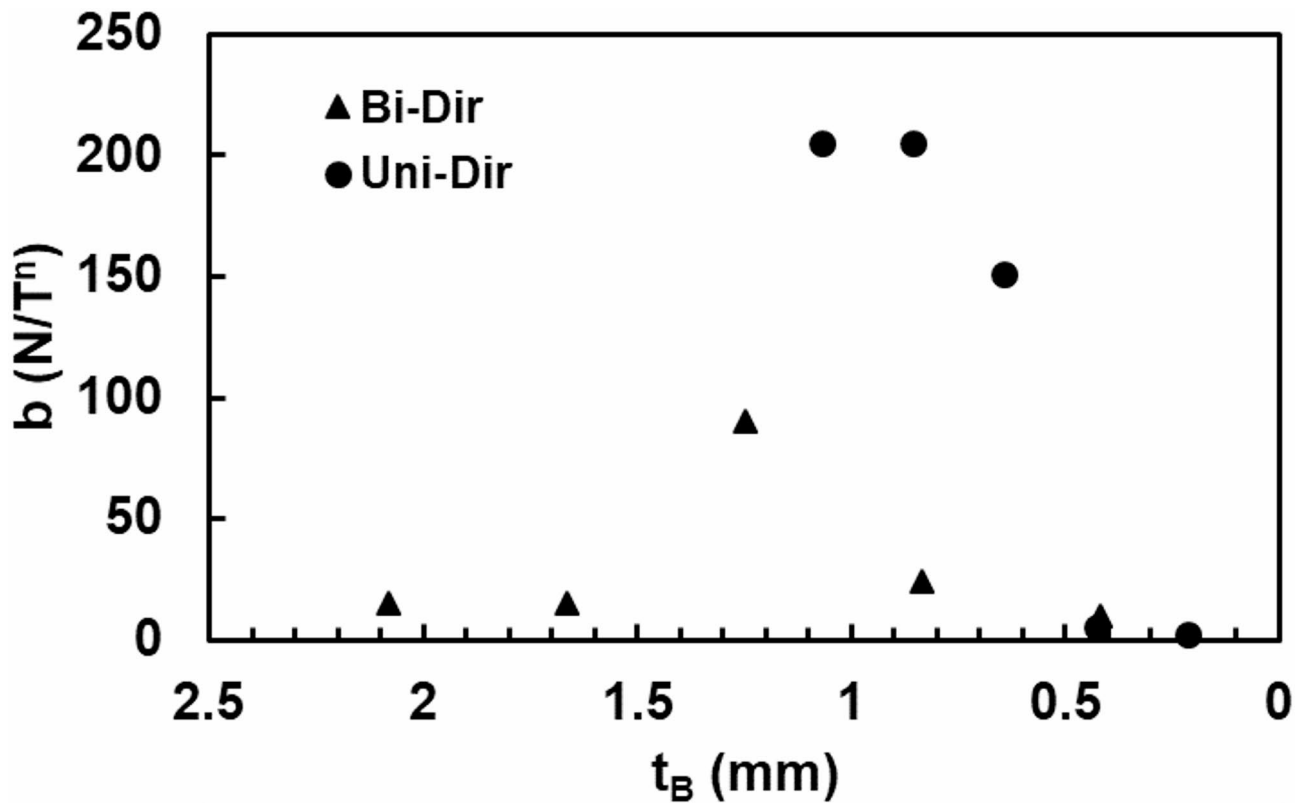
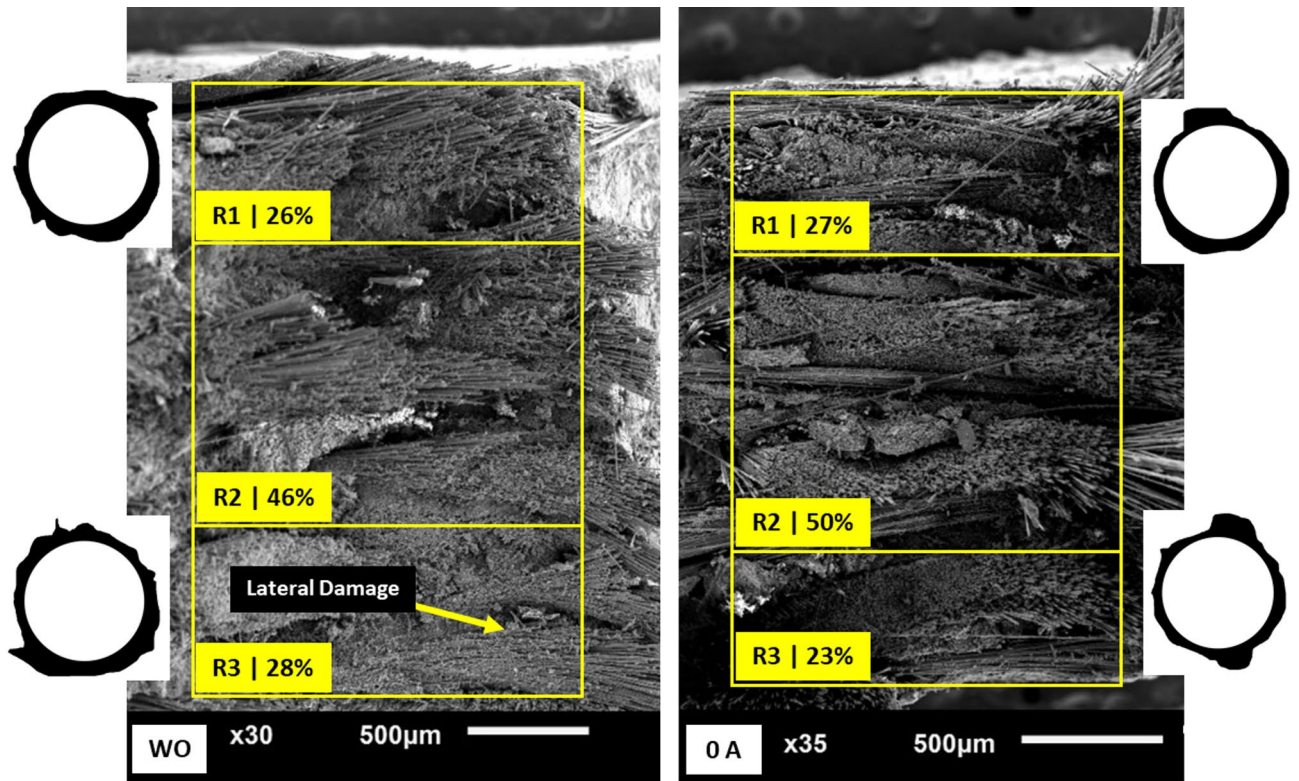


Fig. 13. Variation of magnetic-induced coefficient with bottom layer thickness for Uni and bi-directional CFRP.

distribution show both cases' micro-level damages during the drilling hole. Under the default setup, layer separation is visible due to the sudden impact of thrust force (relates to region 1 in Fig. 9(a) and continues throughout the vertical length. The effect also creates lateral damage. The percentage width can be correlated to areas in Fig. 9(a). The middle region indicates the reduction in inter-layer damage when MRE is used and manifests the decrease in thrust force. However, there is evidence of fibre debonding in region 3, which can affect the overall microstructure of a drilled hole. Thus, using MRE, the inter-layer damages can be controlled, which relates to the absorption of thrust force as MRE behaves as an elastic material. The material loss is visible in both images (Fig. 14).

To draw a firm conclusion about the microstructure observation using an active-backup support, the SEM image of the hole drilled using MRE with 0.48 T is compared with the 0.0 T condition (Fig. 15). The layers of the



**Fig. 14.** Cross-sectional SEM image of the drilled hole of unidirectional CFRP. (WO: default setup, MRE with 0 A ( $B=0.0$  T). R1, R2 and R3 correspond to regions defined in Fig. 9(a).

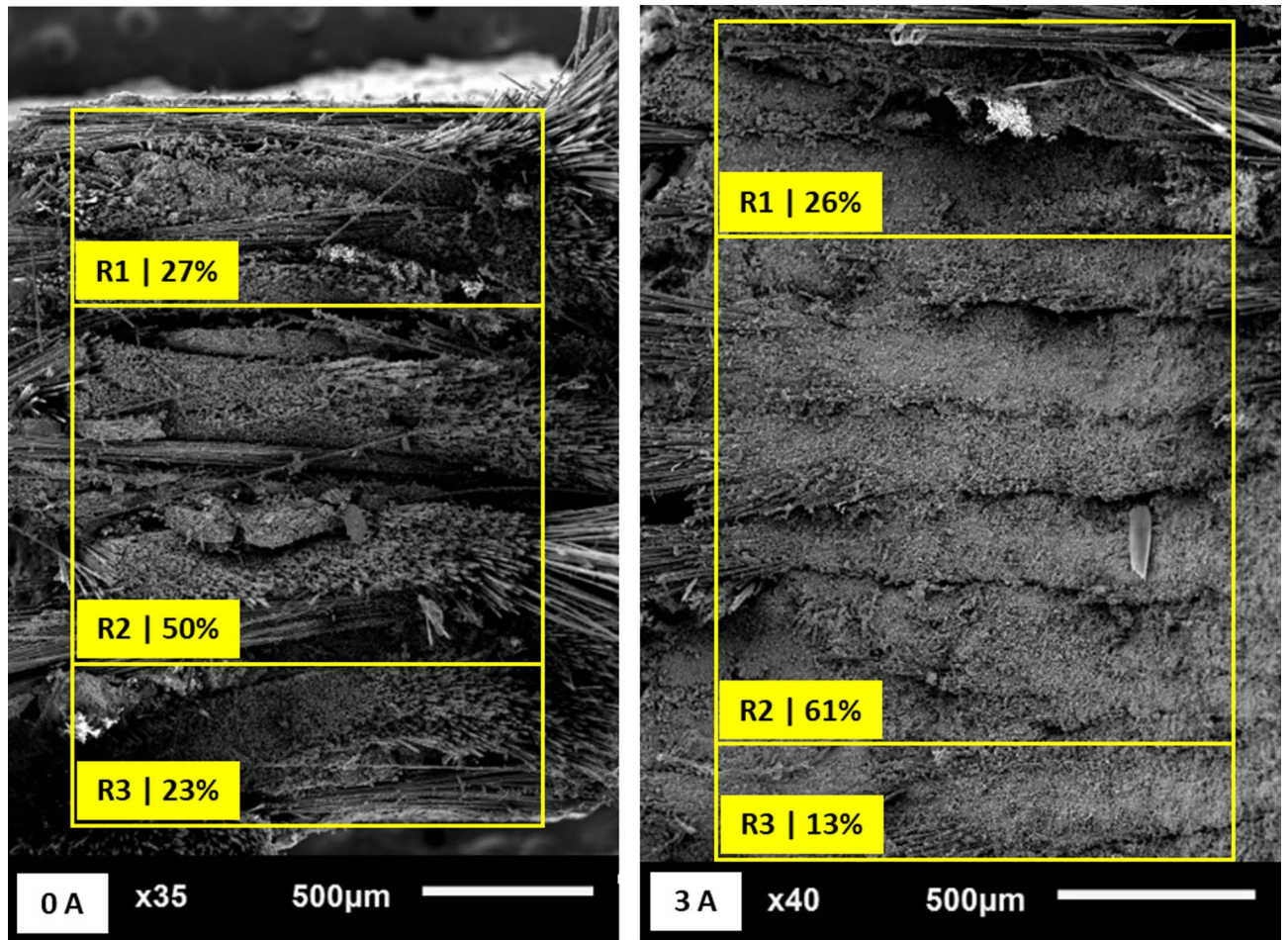
lamina (almost 61% of the total structure) are under the active backup, which advocates the effect of reducing thrust force during drilling when a 0.48 T current is applied to MRE. It was also observed that strong fibre bonding is sustained, resulting in a lower loss in the matrix material and lower lateral damage compared to MRE with the 0.0 T condition. An important aspect to mention is that the last lamina layers are in contact when the magnetic field is applied (Fig. 15). No lateral or vertical damage occurred as the drill tools left the material. Thus, it strongly indicates reduced damage during exit (delamination). Therefore, using MRE as an active backup can reduce CFRP's thrust force and microstructural damage.

Figure 16 compares the SEM images of bidirectional CFRP under the default setup and MRE with 0 A. Significant fiber loss (R1) is observed in the default setup compared to drilling with MRE at 0.0 T. Due to the reduction in thrust force, as MRE behaves like an elastic material, fiber debonding is less severe compared to the default setup. The reduction in thrust force also leads to lower vertical damage (R2), but due to thrust force transmissibility, the effect of lateral damage cannot be entirely suppressed (R2). It is evident from Fig. 11 that the elastic properties of MRE influence thrust force as well as lateral damage at entry and exit levels. The decrease in thrust force helps to maintain the microstructure intake within MRE. The percentage increase in R2 correlates with the elastic properties of MRE.

The influence of the magnetic field on the microstructure damage in bidirectional CFRP during drilling is shown in Fig. 17. An SEM image of the drilling hole using MRE with 3 A reveals a similar observation to unidirectional CFRP drilling using MRE with 0.48 T (Fig. 17). Unlike drilling MRE with 0.0 T, no layer separation was found when 0.48 T current was applied. Layer stacking refers to the intake at the entry level (R1) and exit level (R3). The microstructure is saved compared to the 0.0 T case (R2). There is a significant enhancement in the R2 region when a 0.48 T magnetic field is applied. Thus, the active backup force reduces the lower layer debonding and the lack of evidence of lateral damage results in lower drilling-induced damage. The higher percentage of R2 region enhancement compared to unidirectional CFRP relates to higher cross-link bonding in bidirectional CFRP. However, it must be noted that the change in slope in Region 1 and Region 3 is different for both CFRP when thrust force measurements were carried out.

## Conclusion

This work uses unidirectional and bidirectional CFRP to study the delamination effect caused by thrust force during drilling. MRE is developed using EIP-based iron particles to reduce the impact of delamination by suppressing the thrust force. Thrust force is measured using a piezoelectric dynamometer. Thrust force is reduced for both types of composite when the MRE-based active backup isolator was tested in both passive (without current) and active mode (at 0.48 T current), compared to MRE. However, maximum reduction of thrust force was observed using MRE with 0.48 T.



**Fig. 15.** Cross-sectional SEM image of the drilled hole of unidirectional CFRP with MRE as active back-up at magnetic field of 0.0 T (0 A) and 0.48 T (3 A). R1, R2 and R3 correspond to regions in Fig. 9(a).

A mechanism with an empirical relation was developed to explain the observed variation in thrust force with the magnetic field in the last five layers. The relation incorporates the elastic and magnetic field contributions of MRE. The results indicate that as the magnetic field increases, the field-induced thrust force is nearly twice as high for unidirectional CFRP compared to bi-directional. However, the influence of the field-induced thrust force begins at half the thickness of the CFRP. A detailed investigation is needed to understand the observed effect.

SEM analysis is conducted to understand the effect of thrust force on layer-wise damage in both unidirectional and bidirectional composites. From the SEM images of both types of composites, it is evident that with the applied magnetic field, MRE serves as backup support, absorbs thrust during the drilling operation, and minimizes layer damage compared to cases without MRE. For MRE at 0.48 T, separate layers of laminates are visible in the SEM analysis for both cases. However, compared to the case without MRE, MRE at 0.0 T exhibits less damage to the fiber and matrix in both instances. Nevertheless, the increased cross-link bonding between the fiber and the matrix in the bidirectional composite mitigates the damage caused by the drilling process. Additionally, the R2 region in the SEM image of the bidirectional composite shows more damage than that in the unidirectional composite, which supports these claims.

The observed analysis necessitates a detailed study on how the thickness of the unidirectional CFRP contributes to the reduction of magnetic-field-induced thrust force and the applicability of the empirical relation to the entire thickness. The study will help apply drilling holes in fibre composites.

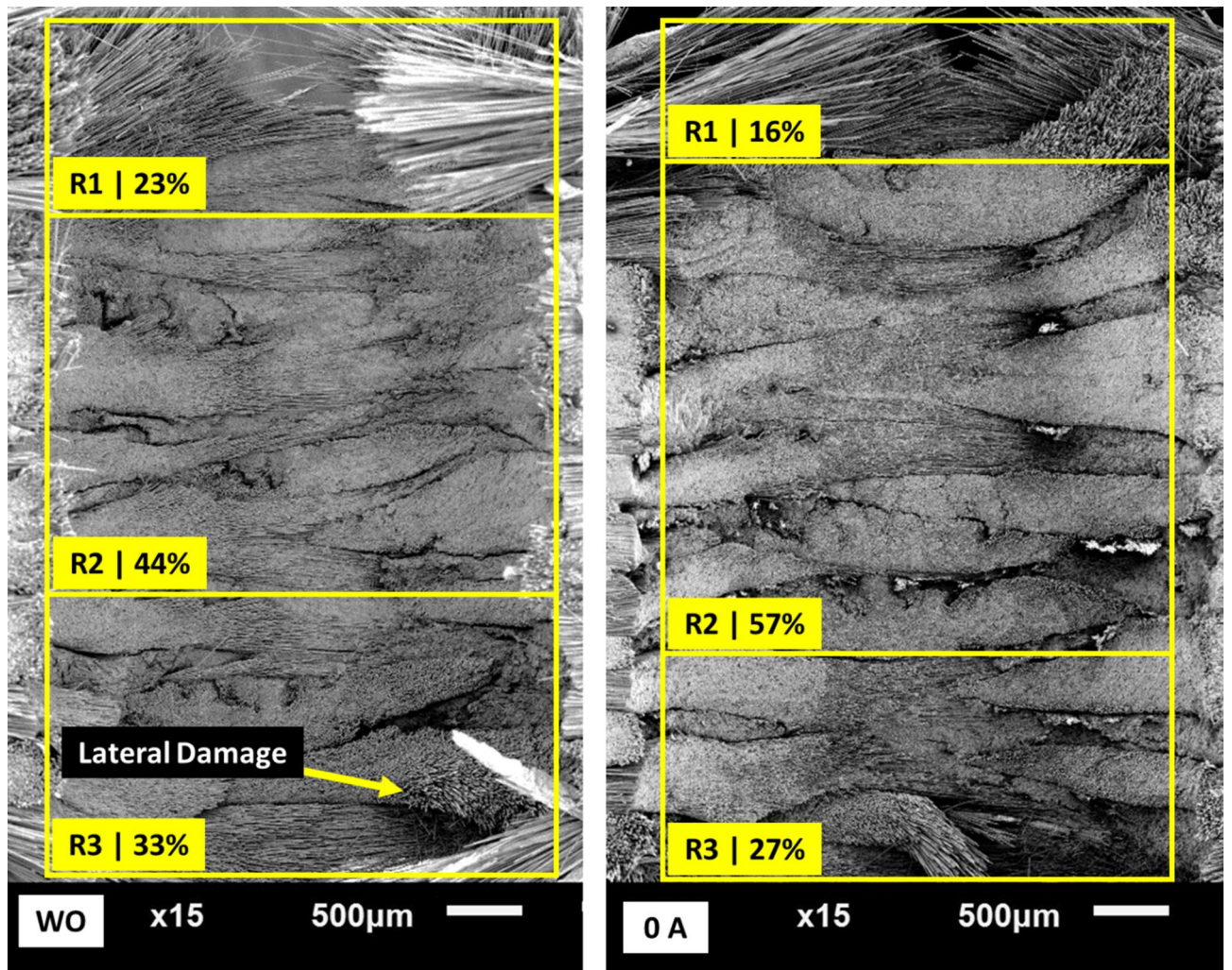
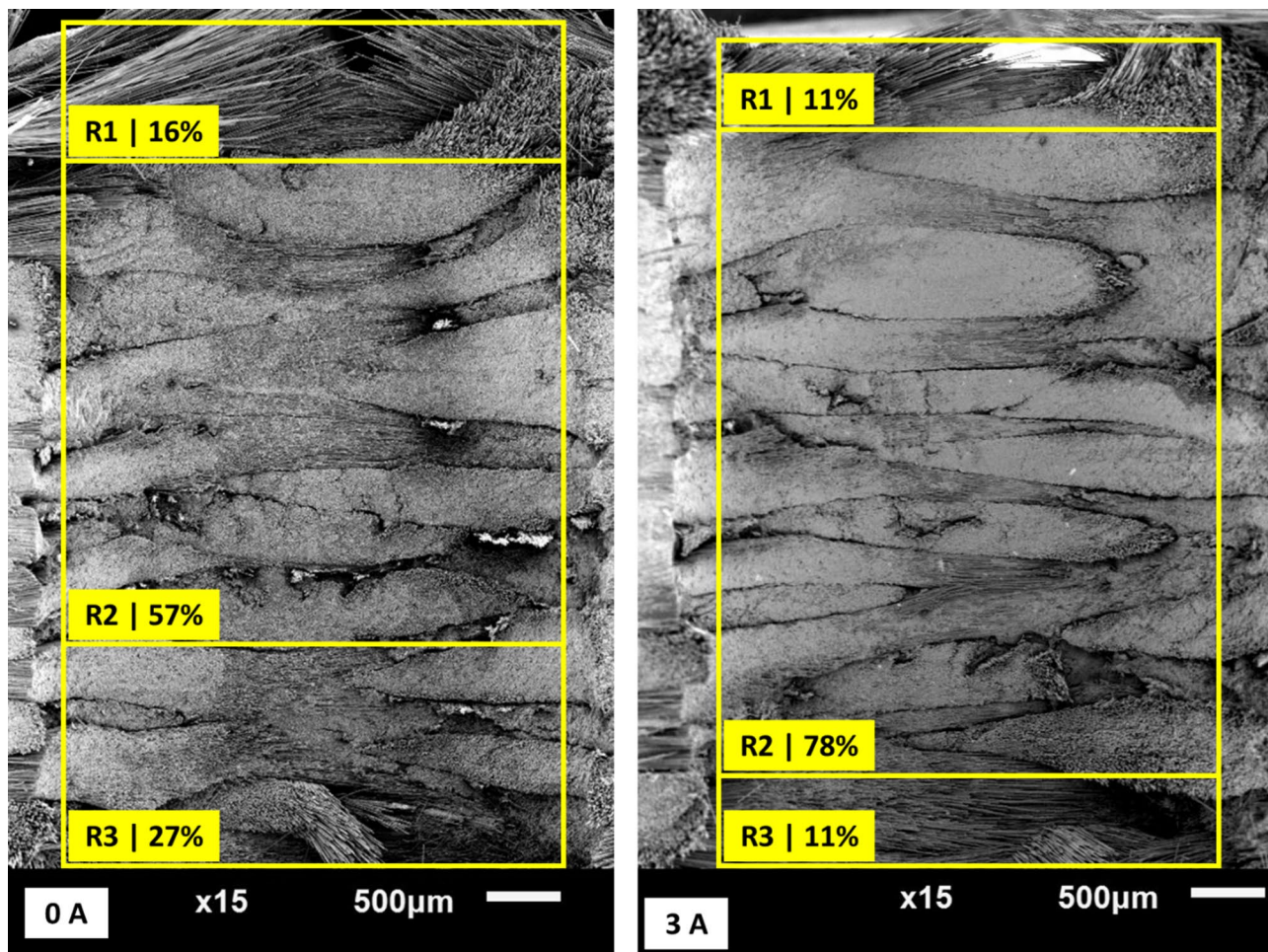


Fig. 16. Crosssectional SEM image of the drilled hole of bidirectional CFRP with MRE. At 0.0 T (0 A). R1, R2 and R3 correspond to regions in Fig. 11(a).



**Fig. 17.** Cross-sectional SEM image of the drilled hole of bidirectional CFRP. (MRE at 0.0 T (0 A) and 0.48 T (3 A). R1, R2 and R3 correspond to regions in Fig. 11(a).

### Data availability

All data generated or analyzed during this study are included in this published article.

Received: 1 February 2025; Accepted: 4 July 2025

Published online: 08 July 2025

### References

- Shyha, I., Soo, S. L., Aspinwall, D. & Bradley, S. Effect of laminate configuration and feed rate on cutting performance when drilling holes in carbon fibre reinforced plastic composites. *J. Mater. Process. Technol.* **210** (8), 1023–1034 (2010).
- Patel, P. & Chaudhary, V. Damage free drilling of carbon fibre reinforced composites—a review. *Australian J. Mech. Eng.* **21** (2), 641–652 (2023).
- Atescan-Yuksekk, Y., Mills, A., Ayre, D., Koziol, K. & Salonitis, K. Comparative life cycle assessment of aluminium and CFRP composites: the case of aerospace manufacturing. *Int. J. Adv. Manuf. Technol.* **131** (7), 4345–4357 (2024).
- Lee, J. H., Ge, J. C. & Song, J. H. Study on burr formation and tool wear in drilling CFRP and its hybrid composites. *Appl. Sci.* **11** (1), 384 (2021).
- Ze, G. K. et al. Challenges associated with drilling of carbon fiber reinforced polymer (CFRP) composites—A review. *Compos. Part. C: Open. Access.* **11**, 100356 (2023).
- Zhang, J., Lin, G., Vaidya, U. & Wang, H. Past, present and future prospective of global carbon fibre composite developments and applications. *Compos. Part. B: Eng.* **250**, 110463 (2023).
- Aamir, M., Giasin, K., Tolouei-Rad, M. & Vafadar, A. A review: drilling performance and hole quality of aluminium alloys for aerospace applications. *J. Mater. Res. Technol.* **9** (6), 12484–12500 (2020).
- Tolouei-Rad, M. & Aamir, M. Analysis of the performance of drilling operations for improving productivity. *Drill. Technol.*, 5–20. (2021).
- Xu, J. et al. A critical review addressing drilling-induced damage of CFRP composites. *Compos. Struct.* **294**, 115594 (2022).
- Patel, P. & Chaudhary, V. Delamination evaluation in drilling of composite materials—A review. *Materials Today: Proceedings*, 56, 2690–2695. (2022).
- Su, F. et al. Comparative analyses of damages formation mechanisms for novel drills based on a new drill-induced damages analytical model. *J. Mater. Process. Technol.* **271**, 111–125 (2019).
- Arul, S., Vijayaraghavan, L., Malhotra, S. K. & Krishnamurthy, R. Influence of tool material on dynamics of drilling of GFRP composites. *Int. J. Adv. Manuf. Technol.* **29**, 655–662 (2006).

13. Jain, S. & Yang, D. C. H. Effects of feedrate and chisel edge on delamination in composite drilling. *J. Eng. Ind.* **115**, 398–405 (1993).
14. König, W., Wulf, C., Grass, P. & Willerschied, H. Machining of Fiber reinforced plastics. *Annals CIRP*. **34** (2), 537–548 (1985).
15. Brinksmeier, E., Fangmann, S. & Rentsch, R. Drilling of composites and resulting surface integrity. *Annals CIRP*. **60** (1), 57–60 (2011).
16. Teti, R. Machining of composite materials. *Annals CIRP*. **51** (2), 611–634 (2002).
17. Franke, V. & Aurich, J. Drilling of long Fiber reinforced Thermoplastics – Influence of the cutting edge on the machining results. *Annals CIRP*. **60** (1), 65–68 (2011).
18. Schulze, V., Becke, C., Pabst, R. & Weule, H. Specific machining forces and resultant force vectors for machining of reinforced plastics. *Annals CIRP*. **60** (1), 69–72 (2011).
19. Stein, J. M. & Dornfeld, D. A. Burr formation in drilling miniature holes. *Annals CIRP*. **46** (1), 63–66 (1997).
20. Xu, J., Geier, N., Shen, J., Krishnaraj, V. & Samsudeensadham, S. A review on CFRP drilling: fundamental mechanisms, damage issues, and approaches toward high-quality drilling. *J. Mater. Res. Technol.* **24**, 9677–9707 (2023).
21. Geng, D. et al. Delamination formation, evaluation and suppression during drilling of composite laminates: A review. *Compos. Struct.* **216**, 168–186 (2019).
22. Liu, M. et al. Cryogenic minimum quantity lubrication machining: from mechanism to application. *Front. Mech. Eng.* **16** (4), 649–697 (2021).
23. Wang, C., Cheng, K., Rakowski, R., Greenwood, D. & Wale, J. Comparative studies on the effect of pilot drillings with application to high-speed drilling of carbon fibre reinforced plastic (CFRP) composites. *Int. J. Adv. Manuf. Technol.* **89**, 3243–3255 (2017).
24. Gao, T. et al. Carbon fiber reinforced polymer in drilling: from damage mechanisms to suppression. *Compos. Struct.* **286**, 115232 (2022).
25. John, K. M. & Kumaran, S. T. Backup support technique towards damage-free drilling of composite materials: A review. *Int. J. Lightweight Mater. Manuf.* **3** (4), 357–364 (2020).
26. Dogrusadik, A. & Kentli, A. Experimental investigation of support plates' influences on tool wear in micro-drilling of CFRP laminates. *J. Manuf. Process.* **38**, 214–222 (2019).
27. Shyha, I. S., Aspinwall, D. K., Soo, S. L. & Bradley, S. Drill geometry and operating effects when cutting small diameter holes in CFRP. *Int. J. Mach. Tools Manuf.* **49** (12–13), 1008–1014 (2009).
28. Wang, G. D., Melly, S. K. & Li, N. Using dampers to mitigate thrust forces during carbon-fibre reinforced polymer drilling: experimental and finite element evaluation. *J. Reinf. Plast. Compos.* **37** (1), 60–74 (2018).
29. John, K. M., Kumaran, S. T., Kurniawan, R. & Ahmed, F. Evaluation of thrust force and delamination in drilling of CFRP by using active spring restoring backup force. *Mater. Today: Proc.* **49**, 269–274 (2022).
30. Tsao, C. C., Hocheng, H. & Chen, Y. C. Delamination reduction in drilling composite materials by active backup force. *CIRP Ann.* **61** (1), 91–94 (2012).
31. Hocheng, H., Tsao, C. C., Liu, C. S. & Chen, H. A. Reducing drilling-induced delamination in composite tube by magnetic colloid back-up. *CIRP Ann.* **63** (1), 85–88 (2014).
32. Du, H., Li, W. & Zhang, N. Semi-active variable stiffness vibration control of vehicle seat suspension using an mrelastomer isolator. *Smart Mater. Struct.* **20** (10), 105003 (2011).
33. Bastola, A. K. & Hossain, M. A review on magneto-mechanical characterizations of magnetorheological elastomers. *Compos. Part. B: Eng.* **200**, 108348 (2020).
34. Yang, C. Y., Fu, J., Yu, M., Zheng, X. & Ju, B. X. A new magnetorheological elastomer isolator in shear–compression mixed mode. *J. Intell. Mater. Syst. Struct.* **26** (10), 1290–1300 (2015).
35. Harne, R. L., Deng, Z. & Dapino, M. J. Adaptive magnetoelectric metamaterials: A new class of magnetorheological elastomers. *J. Intell. Mater. Syst. Struct.* **29** (2), 265–278 (2018).
36. Wang, S. et al. Structure design and optimization of MRE vibration isolator. *Appl. Sci.* **14** (24), 11755 (2024).
37. Patel, P. et al. Delamination and thrust force mitigation during drilling of unidirectional carbon fibre-reinforced plastic laminate using magnetorheological elastomer. *Smart Mater. Struct.* **33** (11), 115015 (2024).
38. Patel, P. & Chaudhary, V. Investigation of Drilling Parameters on Carbon Fiber Reinforced Polymer (CFRP). *Industry 5.0 and Paradigm Shift—Emerging Challenges*, 271. (2023).
39. Patel, P. & Chaudhary, V. Numerical prediction of critical thrust force during drilling in polymer composites—A review. *Materials Today: Proceedings*. (2023).
40. Dharan, C. K. H. Fracture mechanics of composite materials. (1978).
41. Zhang, L. B., Wang, L. J. & Liu, X. Y. A mechanical model for predicting critical thrust forces in drilling composite laminates. *Proc. Institution Mech. Eng. Part B: J. Eng. Manuf.* **215** (2), 135–146 (2001).
42. Timoshenko, S. & Woinowsky-Krieger, S. Theory of plates and shells. (1959).
43. Jones, R. M. *Mechanics of Composite Materials* (CRC, 2018).
44. Daniel, I. M., Ishai, O., Daniel, I. M. & Daniel, I. *Engineering Mechanics of Composite Materials* (Vol3pp. 256–256 (Oxford University Press, 1994).
45. Ho-Cheng, H. & Dharan, C. K. H. Delamination during drilling in composite laminates. *J. Eng. Ind.*, **112**(3), 236–239. <https://doi.org/10.1115/1.2899580> (1990).
46. Patel, P. & Chaudhary, V. Critical thrust force prediction in unidirectional CFRP drilling: an analytical modeling approach. *Proceedings of the Institution of Mechanical Engineers, Part C: Journal of Mechanical Engineering Science*, **238**(10), 4513–4525. (2024).
47. Patel, S. R., Upadhyay, R. V. & Patel, D. M. Life-cycle evaluation of anisotropic particle-based magnetorheological fluid in MR brake performance. *Braz. J. Phys.* **50**, 525–533 (2020).
48. Aamir, M., Tolouei-Rad, M., Giasin, K. & Nosrati, A. Recent advances in drilling of carbon fiber-reinforced polymers for aerospace applications: A review. *Int. J. Adv. Manuf. Technol.* **105**, 2289–2308 (2019).

## Acknowledgements

The authors would like to acknowledge Charotar University of Science and Technology (CHARUSAT) for their support.

## Author contributions

Conceptualization: P.P., R.U., and S. P.; methodology: P.P., R.U., S.P. and D. P.; formal analysis, investigation, and writing—original draft preparation P.P., R.U., and S. P.; writing—review and editing, P.P., R.U., S.P. and D. P.; supervision, R.U., V. C.; All authors have read and agreed to the published version of the manuscript.

## Declarations

### Competing interests

The authors declare no competing interests.

### Additional information

**Correspondence** and requests for materials should be addressed to P.P.

**Reprints and permissions information** is available at [www.nature.com/reprints](http://www.nature.com/reprints).

**Publisher's note** Springer Nature remains neutral with regard to jurisdictional claims in published maps and institutional affiliations.

**Open Access** This article is licensed under a Creative Commons Attribution-NonCommercial-NoDerivatives 4.0 International License, which permits any non-commercial use, sharing, distribution and reproduction in any medium or format, as long as you give appropriate credit to the original author(s) and the source, provide a link to the Creative Commons licence, and indicate if you modified the licensed material. You do not have permission under this licence to share adapted material derived from this article or parts of it. The images or other third party material in this article are included in the article's Creative Commons licence, unless indicated otherwise in a credit line to the material. If material is not included in the article's Creative Commons licence and your intended use is not permitted by statutory regulation or exceeds the permitted use, you will need to obtain permission directly from the copyright holder. To view a copy of this licence, visit <http://creativecommons.org/licenses/by-nc-nd/4.0/>.

© The Author(s) 2025